ADVANCED MATERIALS TECHNOLOGIES
www.advmattechnol.de

Highly Stable Artificial Synapses Based on Ferroelectric Tunnel Junctions for Neuromorphic Computing Applications

*Sungmun Song, Woori Ham, Gyuil Park, Wonwoo Kho, Jisoo Kim, Hyunjoo Hwang, Hyo-Bae Kim, Hyunsun Song, Ji-Hoon Ahn, and Seung-Eon Ahn**

Owing to the limited processing speed and power efficiency of the current computing method based on the von Neumann architecture, research on artificial synaptic devices for implementing neuromorphic computing capable of parallel computation is accelerating. The potential application of artificial synapses composed of ferroelectric tunnel junctions based on metal–hafnium zirconium oxide–metal structure for neuromorphic computing is investigated. Multiple resistance levels are implemented through partial polarization switching control, and synaptic plasticity is successfully imitated based on a high level of device stability and reproducibility. In addition, this device exhibits linear symmetric long-term potentiation and long-term depression using a highly variable pulse driving scheme. Finally, the artificial neural network applied with this synaptic device shows high classification accuracy (95.95%) for the Mixed National Institute of Standards and Technology handwritten digits.

1. Introduction

Due to the proliferation of information devices, annual data production is increasing exponentially, and it is expected that 170 ZB of data will be produced in 2025.[1] In addition, the development of state-of-the-art learning applications, such as artificial intelligence, autonomous driving, and voice and image recognition, based on the produced big data is accelerating. However, as the amount of data to be processed increases, the current von Neumann computing architecture, which is based on serial operations, becomes inefficient in terms of operation speed and energy consumption,[2,3] which limits the scalability of large-scale network applications. As a solution to the bottleneck of the von Neumann architecture, neuromorphic computing, which mimics the human brain to perform complex computations through massively parallel computations, has been proposed. The human brain consists of more than 10^{11} neurons and more than 10^{14} synapses. The neurons and synapses are connected in parallel to perform memory, computation, reasoning, and learning simultaneously, even with a low power of ≈20 W. In particular, the human brain learns by reconstructing the connection strength between synapses, called synaptic plasticity. As a result, developing artificial synaptic devices capable of mimicking synaptic plasticity for the implementation of artificial neural networks (ANNs) is a critical challenge. Recently, it has been reported that memristors, which have multiple resistance states that can be continuously modulated by an external electrical stimulus, can mimic the function of biological synapses.[4] Various devices, such as resistive switching memory,[5–8] phase change memory,[9–11] ferroelectric memory,[12–15] and others,[16–18] have been proposed as candidates for high-efficiency and high-performance memristors. A common feature of these devices is that they mimic synaptic weights by expressing values between 0 and 1 in an analog form, as opposed to the current digital-based information communication devices that only use 0 and 1. Among them, the $HfZrO_2$ (HZO)-based ferroelectric tunnel junction (FTJ) device controls the partial polarization reversal of a ferroelectric thin film to mimic the synaptic weight. Consequently, it implements a multi-resistance state between the high-resistance state (HRS) and low-resistance state (LRS).[19,20] In addition, synaptic characteristics can be secured using a two-terminal metal-semiconductor-metal (MFM) device structure, which has the advantage of being able to design for high integration of $4F^2$. In this study, we investigated the synaptic properties of the HZO FTJ device with an MFM structure for neuromorphic computing applications. HZO ferroelectric thin films with a non-perovskite structure are appropriate for ultra-thin three dimensional capacitors, because they exhibit ferroelectric properties even in a thin film close to 1 nm and have large bandgaps. Moreover, Ferroelectric doped-HfO_2 is considered an alternative to ferroelectric perovskites because of its full CMOS (complementary metal–oxide–semiconductor) process compatibility, high scalability and easy stabilization

S. Song, W. Ham, H. Song, S.-E. Ahn
Department of Nano & Semiconductor Engineering
Korea Polytechnic University
Siheung, Gyeonggi-do 15073, Republic of Korea
E-mail: seahn@kpu.ac.kr
G. Park, W. Kho, J. Kim, H. Hwang, S.-E. Ahn
Department of IT · Semiconductor Convergence Engineering
Korea Polytechnic University
Siheung, Gyeonggi-do 15073, Republic of Korea
H.-B. Kim, J.-H. Ahn
Department of Material Science and Chemical Engineering
Hanyang University
Ansan 15588, Republic of Korea

The ORCID identification number(s) for the author(s) of this article can be found under https://doi.org/10.1002/admt.202101323.

DOI: 10.1002/admt.202101323

of ferroelectricity by proper doping. The polarization and tunneling current characteristics in the microscopic structure were analyzed by piezoresponse force microscopy (PFM) and conductive atomic force microscopy (C-AFM). In addition, the switching dynamics were analyzed based on the nucleation-limited switching (NLS) model. Long-term plasticity characteristics were secured by an incremental voltage scheme, and the linearity and symmetry of the multi-conductance state were analyzed. Based on the experimental data, an ANN was simulated using a small image (8 × 8 pixels) dataset from the University of California at Irvine (UCI)[21] and a large image (28 × 28 pixels) dataset from the Mixed National Institute of Standards and Technology (MNIST).[22] The recognition accuracy was 95.82% for the small image dataset and 95.95% for the large image dataset. As a result, we propose that HZO FTJ-based memristors can be applied as synaptic devices for stable and efficient ANNs.

2. Results and Discussion

A 10 nm thick HZO ferroelectric thin film was deposited on a $TiN/SiO_2/Si$ substrate using an atomic layer deposition (ALD) process to create the FTJ device used to implement the artificial synaptic device. TiN was then deposited as the top electrode, and rapid thermal annealing (RTA) was performed. The HZO FTJ device exhibits a typical hysteresis loop, which is a fundamental characteristic of a ferroelectric, and has a remnant polarization of ≈19 μC cm^{-2} (Figure S1, Supporting Information). Furthermore, it has different tunneling currents depending on the upward and downward polarization (Figure S2, Supporting Information). The electron transport mechanism of the FTJ device is dominated by Fowler–Nordheim tunneling (FNT) for both upward and downward polarization (Figure S3, Supporting Information). Tunneling properties can be modulated depending on the polarization direction, producing tunneling electro-resistance (TER) effect, which refers to two states of electrical resistance. The TER effect is related to variations in the effective potential barrier owing to asymmetric charge screening lengths at the ferroelectric/electrode interface.[15,23,24] PFM analysis was performed to demonstrate the ferroelectricity of the microscopic structure of the HZO thin film (**Figure 1**a). As shown in the schematic, the polarization of the HZO thin film was reversed by a direct current (DC) bias, and the piezoresponse force was measured using an alternating current (AC) signal applied by the lock-in amplifier. Figure 1b shows the phase (upper panel) and amplitude (lower panel) measured at a local region of the HZO thin film. The phase and amplitude in the localized region exhibited a clear hysteresis behavior between the upward and downward polarization. A domain pattern was formed by alternately applying a DC bias of +10 and −10 V while simultaneously reducing the scan area at uniform intervals from the outline of the domain (Figure S4, Supporting Information). Figure 1c,d shows the scan results using an AC bias of +1 V. The pattern of the domain can be clearly distinguished in both the phase and amplitude signals. Figure 1e shows the polarization direction-dependent current of the HZO thin film measured by C-AFM. A DC bias of +8 and −8 V was applied alternately starting on the left to form a domain pattern. A DC bias of +1 V was applied to scan the domain pattern region (blue shaded area) to map the current characteristics (red line at the bottom). The HRS and LRS match the pattern of the formed domain, and both states have different current levels from that of the original state. Based on the difference in polarization characteristics and tunneling current demonstrated by the PFM and C-AFM results, the 10 nm thick HZO thin film has excellent ferroelectricity.

HZO ferroelectric thin films fabricated through the ALD process have a polycrystalline structure.[25] Different domains have different nucleation rates owing to defects at the interface

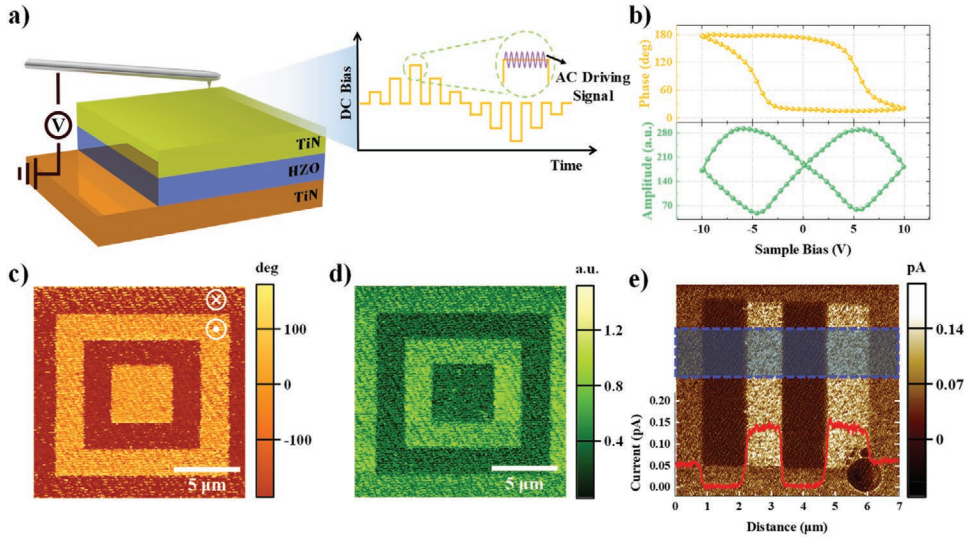

Figure 1. Schematic representation and microscopic characterization of HZO FTJ devices. a) Structure of the TiN/HZO/TiN FTJ device and PFM measurement scheme. b) Local ferroelectric properties: PFM phase (upper panel) and amplitude (lower panel) hysteresis loops of the TiN/HZO/TiN structure. PFM measurements of the c) phase and d) amplitude of the HZO/TiN structure after domain patterning with opposite polarities. e) C-AFM image of the of the HZO/TiN structure. The inset data (red line) is the current mapping characteristics of the blue shaded area.

or in the interior of the polycrystalline ferroelectric thin film.[26–28] Therefore, the polarization reversal rate is a distribution rather than a single value.[29,30] Owing to the distributed switching characteristics, the resistance can be varied gradually between the LRS and HRS, and this analog implementation of the resistance state is the factor most directly related to weight implementation, which is the core element of artificial synaptic devices. This gradual change in resistance can be applied to the parallel resistance model and expressed by[31]

$$\frac{1}{R}=\frac{(1-S)}{R_{LRS}}+\frac{S}{R_{HRS}} \tag{1}$$

where R is the current state of resistance, R_{LRS} is the lowest resistance state in an upwardly polarized state (ON state), and R_{HRS} is the highest resistance state in a downwardly polarized state (OFF state). S is the ferroelectric polarization state (fully upward, $S = 0$; fully downward, $S = 1$). The domain polarization switching dynamics were investigated to optimize the synaptic weights in a restricted memory window (between the HRS and LRS) and accurately control them with external stimuli. The domain nucleation process and domain wall motion are well explained by the NLS model based on the polycrystalline perovskite ferroelectric thin film.[32,33] Since the HfO_2-based ferroelectric thin film also has a polycrystalline structure, the domain behavior can be investigated with the NLS model.[34,35] The polarization reversal region S is expressed by[29]

$$S=\int_{-\infty}^{+\infty}\left\{1-\exp\left[-\left(\frac{t}{t_0}\right)^n\right]\right\}\times F\left(\log t_0\right)d\left(\log t_0\right) \tag{2}$$

where n is the effective dimension (2 is typically used for thin films), t_0 is the mean switching time, and $F(\log t_0)$ can be described as a Lorentz distribution.

$$F\left(\log t_0\right)=\frac{A}{\pi}\times\left[\frac{w}{\left(\log t-\log t_0\right)^2+w^2}\right] \tag{3}$$

where A is the normalization constant, and w is the half width at half maximum. Figure S5 (Supporting Information) shows the change in the dynamic resistance over the pulse duration with different pulse amplitudes. Prior to each measurement, a −3 V, 100 µs pulse was applied to ensure that the polarization of the ferroelectric thin film was in the ON state. When the applied pulse amplitude was small, the modulation in resistance gradually increased with increasing pulse width, and as the applied pulse amplitude increased, a larger modulation in resistance occurred, even with a small pulse width. Under the fastest driving conditions, the energy consumption per programming pulse was calculated to be between 445 and 1030 fJ (Figure S6, Supporting Information). By substituting these dynamic resistance changes into Equation (1), S was extracted, and the values are displayed in **Figure 2**a. The experimentally determined S values and those calculated by the NLS model (fitted line) using Equation (2) agree well, indicating that the switching characteristics are well explained by the NLS model. The Lorentz distributions at different pulse amplitudes, calculated using Equation (3), are shown in Figure 2b. For larger pulse amplitudes, polarization switching occurred earlier and had a narrower distribution. Furthermore, polarization switching occurred more slowly, and the total amount of the switching distribution decreased as the pulse amplitude decreased. Figure 2c shows plots of log t_0 versus $1/E$ (upper panel) and w versus $1/E^2$ (lower panel) for different pulse amplitudes. The results were verified to have a linear slope. The upper panel is consistent with Merz's law ($t_0 \propto \exp(E_0/E)$), and the activation field (E_0) is 0.67 V nm^{-1}.[36] The activation field is a unique property that can quantify the switching behavior of ferroelectric thin films.[37] After rescaling S by (log t − log t_0)/w, all the curves converge to a single arc tangent function, as shown in Figure 2d. This indicates that the switching dynamics are predominately controlled by the Lorentz distribution in the ferroelectric thin film, which determines the operation of the device.

To investigate the multiple resistance characteristics of HZO FTJ devices with different pulse amplitudes and widths, resistance–voltage (R–V) hysteresis loops were analyzed. In general, a fixed pulse driving scheme and a variable pulse driving scheme can be used to implement synaptic weights. Among them, the fixed pulse driving scheme is known to be more useful in implementing the driving module in a circuit in practical applications. However, in this study, a variable pulse driving scheme was chosen, which is the most suitable scheme for HZO synaptic devices and has advantages in dynamic range, multiple resistance states, and linearity.[38]

Figure 3a illustrates the effect of the applied pulse amplitude when the pulse width was fixed at 10 µs. As shown in the inset, for multiple resistance level programming, the pulse amplitude was increased from −2.9 $V_{max(-)}$ to $V_{max(+)}$ (1.5, 1.7, 1.9, 2.1, 2.3, 2.9 V) and then decreased again. Resistance was measured at +0.5 V after each program pulse (Figure S13, Supporting Information). $V_{max(+)}$ is the maximum positive voltage, and $V_{max(-)}$ is the maximum negative voltage. When a positive pulse was applied, the polarization was aligned downward (HRS), and when a negative pulse was applied, the polarization was aligned upward (LRS). The device exhibited the same behavior as that observed by C-AFM. In addition, the intermediate state between the LRS and HRS formed by partial polarization reversal was well maintained without decay of resistance until Vth was reached in the opposite direction. Vth is the threshold voltage, which is the voltage at which the resistance begins to vary from LRS to HRS or vice versa. This characteristic implies that analog operation methods represented by multiple resistance states can be implemented. Depending on the amplitude of the last applied pulse in the sequence, the TER changed from ≈50% to 250%. However, the negative saturation resistance and positive Vth were the same. This similar behavior with the same distribution at the same amplitude is consistent with the previous switching distribution characteristics. Figure 3b illustrates the effect of pulse width when the last applied pulse amplitude was fixed at 2.9 V. The width was varied from sequence to sequence, as shown in the inset. |Vth| decreased gradually as the pulse width increased, and eventually, |Vth| became saturated when the pulse width was greater than 10 µs. The HRS increased gradually with increasing pulse width, and TER achieved a maximum of 300% at a pulse width

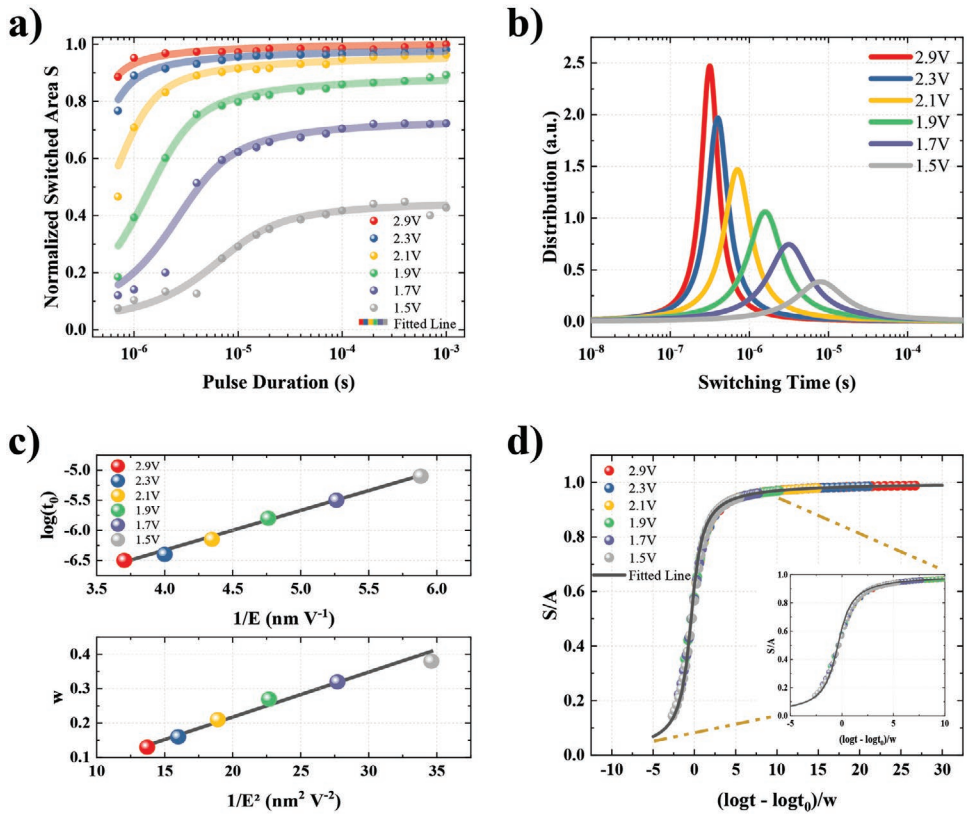

Figure 2. Analysis of the domain switching dynamics of the HZO FTJ device using the NLS model. a) Polarization switching areas as a function of pulse width for various pulse amplitudes. The fitted lines are calculated from the NLS model. b) Lorentz distributions of switching times at different pulse amplitudes extracted from the line in (a). c) Evolution of the mean switching time (upper panel) and half width at half maximum (lower panel) as a function of the pulse amplitude. d) Normalized polarization switching areas using fitting parameters for the NLS model.

of 100 µs. Therefore, the potential barrier can be modulated by varying the pulse width. The above results verify that the analog-type resistance required for synaptic devices can be implemented in the present HZO synaptic device and that the resistance state can be finely adjusted by the amplitude and width of the pulse.

Figure 3c shows the endurance of seven different resistance state sets created through partial polarization reversal. For the endurance performance measurement, the positive direction part of the pulse sequence for the R–V characteristic curve was used as it was to set it to be the same as the resistance value formed in the R–V characteristic curve (Figure 3a). Before applying the programming pulse, the polarization was pre-arranged so that the resistance state of the FTJ could maintain the LRS. During electric field cycling, the endurance of multiple resistance states was confirmed at each desired cycling interval (Figures S13 and S14, Supporting Information). The resistance state cycling was measured with a log scale (10^n, 2×10^n, 4×10^n) and proceeded until 10^7. The resistance state of the HZO synaptic device remained constant without decay and with good reproducibility up to 10^5 cycles. Furthermore, analysis of the characteristics of the first 50 repeated operations indicated that there was a low standard deviation in the complete polarization reversal state (LRS, HRS) (Figure S7, Supporting Information), and as the resistance increased, the standard deviation also increased. After 10^5 cycles, multiple resistance states began to decay, which can be caused by the formation of leakage current paths due to the creation or rearrangement of defects such as oxygen vacancies during electrical cycling. However, the individual resistance states could still be clearly distinguished. Figure 3d displays the retention characteristics to demonstrate the non-volatility in the individual resistance state. The state of the initially measured resistance was maintained for more than 10^5 s without significant loss. Overall, the weak degradation from LRS to HRS could be due to the internal field caused by the asymmetrically formed junction between the top and bottom electrodes and the ferroelectric during processing. As shown in Figure 3a,b, the switching voltage is slightly biased toward the positive voltage. There is an internal electric field in the negative direction, which causes retention loss from LRS to HRS.

Nevertheless, based on extrapolation of the results above 10^5 s, the device is expected to maintain excellent non-volatile characteristics, that is, the resistance state can be clearly distinguished, for up to 10 years. All these results demonstrate that the HZO synaptic device has high reliability and can mimic synaptic properties through partial polarization reversal of domains.

In the human brain, memory is divided into short-term memory (STM) and long-term memory (LTM). When a synapse undergoes a physical or chemical change due to a signal exceeding the threshold voltage between neurons, it

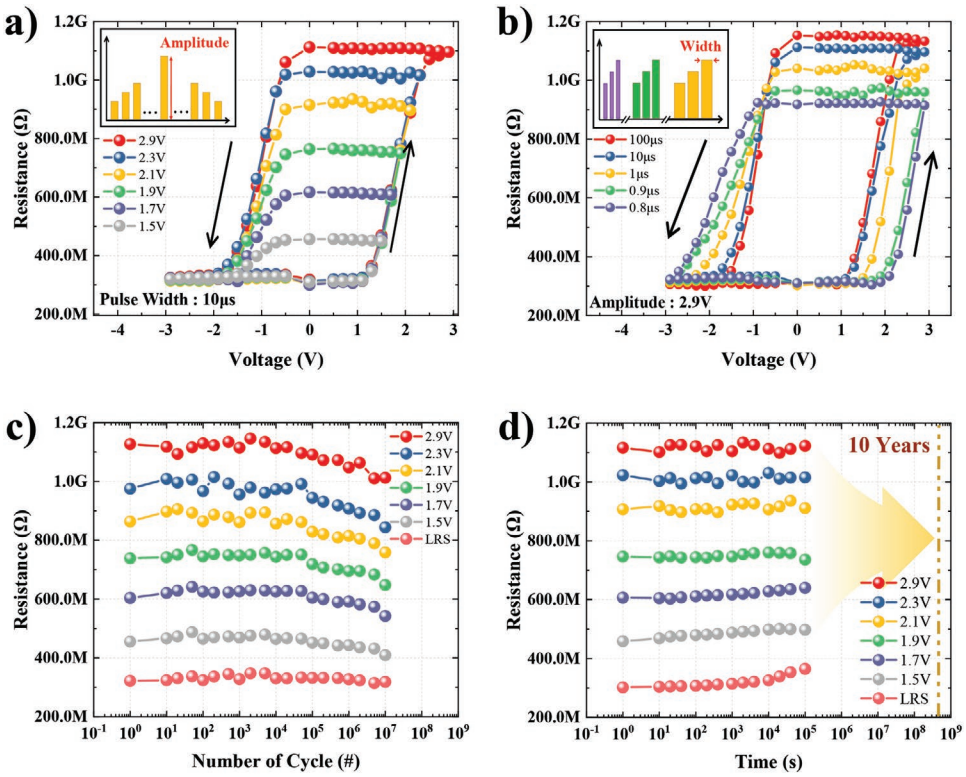

Figure 3. Multiple resistance characteristic and reliability properties. R–V hysteresis loops as functions of a) pulse amplitude and b) pulse width. Experimental parameters were adjusted as shown in the insets of (a) and (b). c) Endurance and d) retention properties in different resistance states demonstrating the non-volatility of the device.

is classified as LTM, and when it does not, it is classified as STM. Physical and chemical changes in synapses are called synaptic plasticity, and synaptic weights are controlled by synaptic plasticity. LTM, which performs functions such as learning, memory, and computation, is regarded as a key design element in neuromorphic computing. LTM consists of long-term potentiation (LTP) and long-term depression (LTD). LTP strengthens the weight of the synapse when information transfer between neurons occurs frequently, and LTD weakens it in the opposite case.

Figure 4a shows the synaptic behavior of the FTJ synaptic device based on the LTP and LTD characteristics. Various programming pulse schemes have been proposed to optimize the synaptic characteristics of artificial synaptic devices.[39] The pulse sequence (LTP, −0.4 to −2.04 V with 0.02 V step; LTD, +1.1 to +2.3 V with 0.02 V step) was repeated for 20 measurements, and the LTP and LTD characteristics were obtained over a conductance range of 0.94–2.73 nS. Conductance state, dynamic range, linearity, and symmetry analyses were performed because these parameters are required to achieve high learning accuracy. Conductance variations occurred even with small changes in the applied pulse amplitude, and 65 and 83 weight levels were implemented for LTP and LTD, respectively. The curve of the synaptic weight (conductance) can be classified as asymmetric or symmetric nonlinear based on the shape of the synaptic weight. Because it matched the behavior of the synaptic weights of the device most closely, symmetric nonlinearity was used for evaluation. The conductance (G) as a function of the normalized pulse number (p) can be expressed as[40]

$$G = A \times \frac{1}{1+\exp\left[-2\nu\left(p-\alpha\right)\right]} + B \tag{4}$$

where

$$A = \left(G_{\max} - G_{\min}\right) \times \frac{\exp\nu + 1}{\exp\nu - 1} \tag{5}$$

$$B = G_{\min} - \frac{\left(G_{\max} - G_{\min}\right)}{\exp\nu - 1} \tag{6}$$

where $G_{\max}$ is the maximum conductance, and $G_{\min}$ is the minimum conductance and α is the center of symmetry. ν is a parameter ($0 \le \nu \le 10$) that characterizes the nonlinearity of the LTP and LTD curves, with values closer to 0 indicating more ideal linear characteristics. Figure 4b shows the fitted line extracted by applying Equation (4) to the mean LTP and LTD curves. The fitted line is in good agreement with the synaptic weights of the HZO synaptic device. The dynamic range ($G_{\max}/G_{\min} \approx 2.928$), LTP ($\alpha = 0.55$, $\nu = 3.13$), and LTD ($\alpha = 0.36$, $\nu = 2.96$) were extracted. Figure 4c shows the characteristics of each curve rather than the mean characteristics. The individual LTP and LTD characteristics have minimal variation from the mean (color line), indicating the excellent reproducibility of the synaptic characteristics. Figure 4d,e displays the statistical

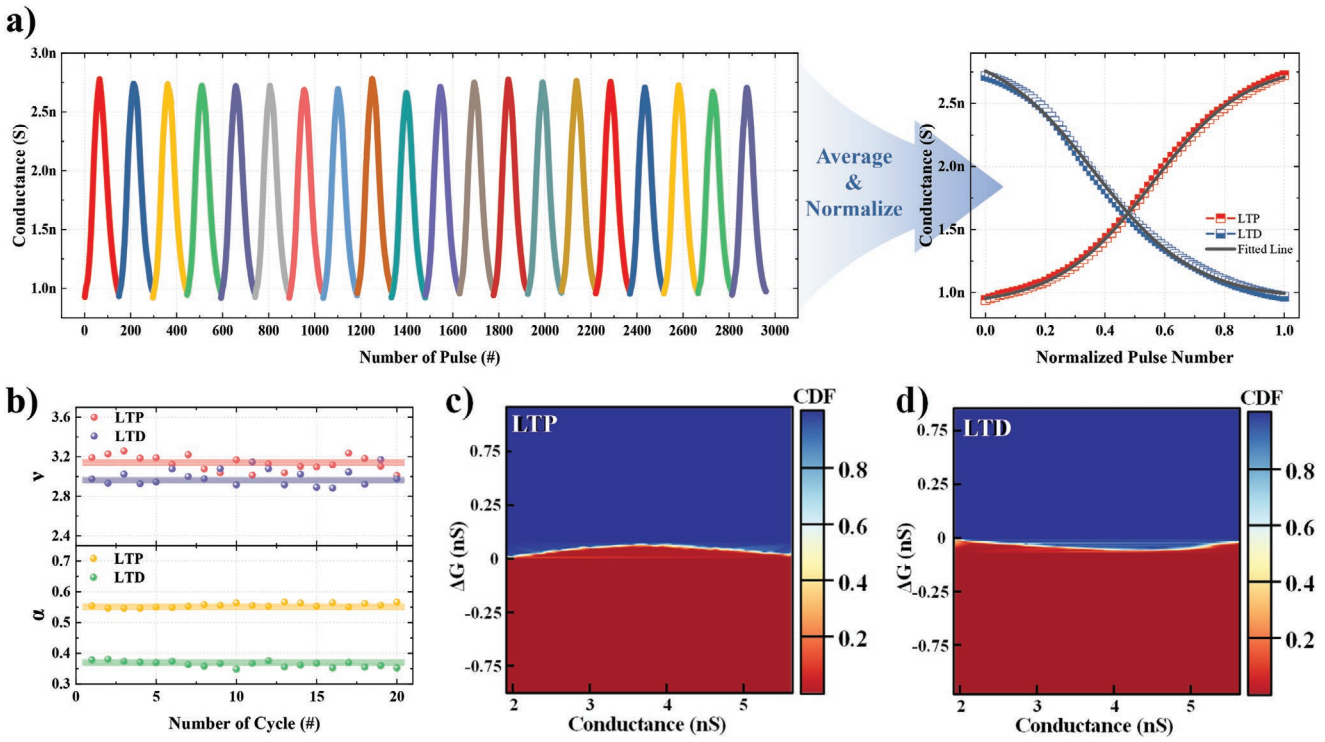

Figure 4. Synaptic characteristics of the HZO FTJ device using an incremental voltage programming pulse scheme. a) LTP and LTD over 20 cycles with the symmetric nonlinearity model. b) Individual nonlinearity (upper panel) and symmetric center points (lower panel) of LTP and LTD over 20 cycles. Deviations in the conductance of c) LTP and d) LTD calculated statistically by applying a cumulative distribution function.

deviations in the conductance of the LTP and LTD curves. For both LTP and LTD, the deviation is distributed over low values.

The HZO synaptic device was used to simulate an ANN to perform supervised learning on two different datasets: a small image dataset (8 × 8 pixels) of handwritten digits from the UCI and a large image dataset (28 × 28 pixels) of handwritten digits from MNIST. As shown in **Figure 5**a, the simulated ANN consisted of three layers: the input layer, a hidden layer, and the output layer. For the small images (8 × 8 pixels), the network size was 64 (input layer) × 36 (hidden layer) × 10 (output layer), where the 64 input neurons correspond to the 8 × 8 UCI data, and the 10 output neurons correspond to 10 classes of digits (0–9). For the large images (28 × 28 pixels), the network size was 784 (input layer) × 300 (hidden layer) × 10 (output layer), where the 784 input neurons correspond to the 28 × 28 MNIST data, and the 10 output neurons correspond to 10 classes of digits (0–9). The simulation was based on a backpropagation algorithm and was conducted using the experimental LTP and LTD characteristics of the HZO synaptic device. In the simulation, a crossbar was composed of an input neuron column (yellow lines) and an output neuron row (red lines) (Figure 5b). The weights were adjusted by interacting with the position of the desired synaptic device and the intersecting input column using programming pulses. The adjusted weights were collected and summed in one output row, and an activation function (sigmoid function) was applied to the summed result; then, the outputs from the input layer act as inputs to the hidden layer. To get outputs in the output layer, same process was applied to the inputs in the hidden layer. All of the weights are trained by cycling through each element of a training dataset, and adjusting weights depending on the backpropagation of errors. Figure S8 (Supporting Information) shows a flowchart of the backpropagation algorithm. In the simulation, weights were randomly initialized with a uniform distribution.[41] The weights were summed from the initialized weights, and errors that might occur during operation in each neural network were calculated probabilistically. Subsequently, one epoch was completed by comparing the values of the calculated and real results and by adjusting the weight by applying a learning rate to the error. Each epoch was performed as described, and the accuracy was verified as the weight was adjusted in each epoch.

Several different learning rates and number of epochs were tested for each dataset (Figure S9, Supporting Information). The optimized learning rates of the small and large image datasets were 0.1 and 0.04, respectively, when the number of epochs was five. For the small image dataset, the ANN was trained with 3823 images from the training datasets, and the recognition accuracy was tested using 1797 images from test datasets for each epoch. After training, the training accuracy for the small image training set was greater than 93% (Figure S10, Supporting Information). After 50 epochs, the HZO synaptic device achieved a test accuracy of 95.3% for the small image test dataset, which is similar to the numerical accuracy of 96.8% (Figure 5c). For the large image dataset, the ANN was trained with 60 000 images from the training dataset for each epoch, and 10 000 images from the test dataset were evaluated for recognition accuracy. After training, the training accuracy reached 92.5% (Figure S11, Supporting Information). The test

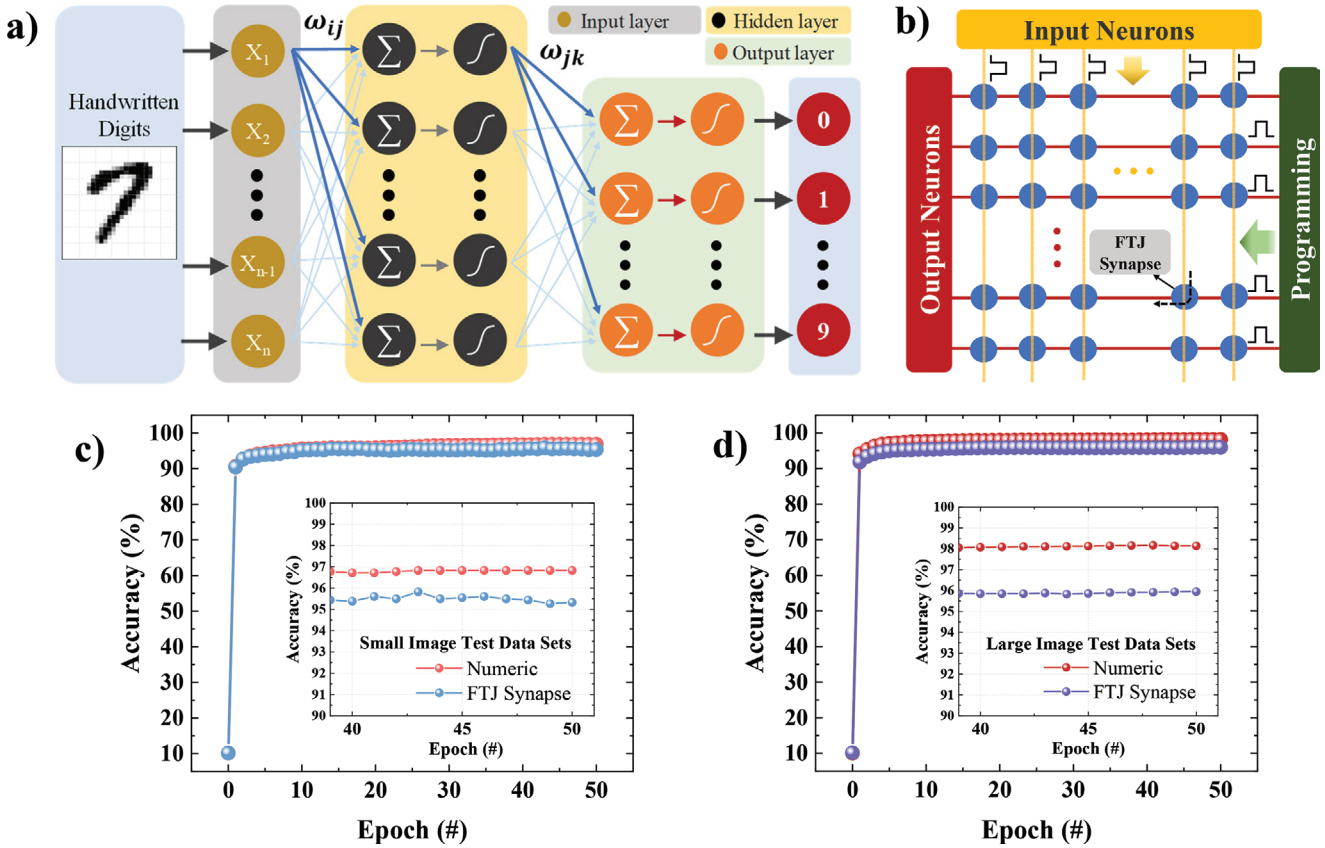

Figure 5. ANN simulation using experimental LTP and LTD properties of the HZO synaptic device. Schematic of a) the three-layer neural network used for the recognition of handwritten digit images and b) the neural core of the crossbar structure used in the simulation. Training accuracy of the HZO synaptic device for the c) small image test datasets and d) large image test datasets.

accuracy for the recognition of the large image test dataset was 95.95% (Figure 5d). This high recognition accuracy is based on the high linearity, symmetry, and reproducibility of the HZO synaptic device.

3. Conclusion

In conclusion, we demonstrated the potential of $HfZrO_2$-based ferroelectric tunnel junctions for artificial synaptic applications. Ferroelectric partial polarization switching and potential barrier modulation were induced by the voltage pulse driving scheme with varying pulse amplitudes or pulse widths. Using this device, it was demonstrated that variable biological synaptic plasticity can be realized at a low power. The LTP and LTD, which were composed of multiple resistance states, exhibited high linearity and symmetry, as well as high stability in endurance and retention tests. The ANN simulated using the FTJ synaptic device with these characteristics demonstrated a very high recognition accuracy of 95.95% for the MNIST handwritten dataset. $HfZrO_2$-based ferroelectrics have attracted considerable attention as next-generation semiconductor materials owing to their high compatibility with CMOS processes, easy stabilization of ferroelectrics by appropriate doping, and excellent scaling potential. In addition, through the demonstration of their possible application in synaptic devices in this study, they will help realize neuromorphic computing applications for future artificial neural networks.

4. Experimental Section

Fabrication: $HfZrO_2$ ferroelectric thin films with a thickness of 10 nm were grown on a $TiN/SiO_2/Si$ substrate by ALD at 300 °C. They were deposited using cyclopentadienyl (Cp)-based cocktail precursors ($Hf[Cp(NMe_2)_3]$ and $Zr[Cp(NMe_2)_3]$) with ozone as the oxidant. The molar ratio of the cocktail precursor was $Hf[Cp(NMe_2)_3]$:$Zr[Cp(NMe_2)_3]$ = 35:65. The top TiN electrode was deposited by RF magnetron sputtering in an Ar and N_2 atmosphere with a circular-patterned hard mask (r = 100 µm). Subsequently, the initial amorphous $HfZrO_2$ thin films were crystallized in a N_2 atmosphere at 600 °C for 40 s to stabilize the ferroelectric phase (Figure S12, Supporting Information).

Characterization: PFM imaging (square test), measurements of the local ferroelectric properties (spectroscopy), and current mapping of the $HfZrO_2$ ferroelectric thin films were performed using AFM (XE7, Park Systems). A lock-in amplifier (SR830 DSP, Stanford Research Systems) was also used for the piezoelectric response. In current mapping, an optional C-AFM module (Ultra-Low Current Amplifier (ULCA), Park Systems) was used to amplify low-level currents. Image analysis software (XEI, Park Systems) was used to analyze the scanned images and process the data.

Electrical Measurements: Electrical measurements were performed using a parameter analyzer (4200A-SCS, Keithley) with a 4225-PMU. For the FTJ device, pulses and DC signals were applied to the top electrodes, and the bottom electrodes were grounded. The low-level

current was measured using a preamplifier connected to the SMU. All measurements were performed at room temperature and were preceded by 50 000 field cycles to rule out the wake-up effect in the pristine state. All pulse measurement schemes used in this study are shown in Figures S13 and S14 (Supporting Information).

Neural Network Simulations: The performance of an ANN based on backpropagation was simulated using the open-source software CrossSim (Crossbar Simulator) written in Python provided by Sandia National Laboratories. In the weight update model, the possible weight values of the device were determined by referring to the lookup table created using experimental values rather than virtual simulations.

Supporting Information

Supporting Information is available from the Wiley Online Library or from the author.

Acknowledgements

This work was supported by the Basic Science Research Program through the National Research Foundation of Korea (NRF) grant funded by the Ministry of Science and ICT (MSIT, Korea) (Nos. NRF-2021R1H1A2014200 and NRF-2020R1G1A1A01006808). This research was also supported by the Korea Institute for Advancement of Technology (KIAT) (No. P0008458, The Competency Development Program for Industry Specialist).

Conflict of Interest

The authors declare no conflict of interest.

Data Availability Statement

The data that support the findings of this study are available in the supplementary material of this article.

Keywords

synaptic devices, HfO_2, ferroelectricity, FTJ, neuromorphic computing

Received: October 8, 2021
Revised: December 4, 2021
Published online: January 13, 2022

[1] D. Reinsel, J. Gantz, J. Rydning, *The Digitization of the World from Edge to Core*, https://www.seagate.com/files/www-content/our-story/trends/files/idc-seagate-dataage-whitepaper.pdf (accessed: April 2019).
[2] M. A. Zidan, J. P. Strachan, W. D. Lu, *Nat. Electron.* **2018**, *1*, 22.
[3] Q. Xia, J. J. Yang, *Nat. Mater.* **2019**, *18*, 309.
[4] D. Kuzum, S. Yu, H. S. Philip Wong, *Nanotechnology* **2013**, *24*, 382001.
[5] M. Prezioso, F. Merrikh-Bayat, B. Hoskins, G. C. Adam, K. K. Likharev, D. B. Strukov, *Nature* **2015**, *521*, 61.
[6] X. Yan, J. Zhao, S. Liu, Z. Zhou, Q. Liu, J. Chen, X. Y. Liu, *Adv. Funct. Mater.* **2018**, *28*, 1705320.
[7] Z. Wang, C. Li, W. Song, M. Rao, D. Belkin, Y. Li, P. Yan, H. Jiang, P. Lin, M. Hu, J. P. Strachan, N. Ge, M. Barnell, Q. Wu, A. G. Barto, Q. Qiu, R. S. Williams, Q. Xia, J. J. Yang, *Nat. Electron.* **2019**, *2*, 115.
[8] Z. Wang, H. Wu, G. W. Burr, C. S. Hwang, K. L. Wang, Q. Xia, J. J. Yang, *Nat. Rev. Mater.* **2020**, *5*, 173.
[9] I. Boybat, M. Le Gallo, S. R. Nandakumar, T. Moraitis, T. Parnell, T. Tuma, B. Rajendran, Y. Leblebici, A. Sebastian, E. Eleftheriou, *Nat. Commun.* **2018**, *9*, 2514.
[10] W. Zhang, R. Mazzarello, M. Wuttig, E. Ma, *Nat. Rev. Mater.* **2019**, *4*, 150.
[11] J. Feldmann, N. Youngblood, C. D. Wright, H. Bhaskaran, W. H. P. Pernice, *Nature* **2019**, *569*, 208.
[12] N. K. Upadhyay, H. Jiang, Z. Wang, S. Asapu, Q. Xia, J. Joshua Yang, *Adv. Mater. Technol.* **2019**, *4*, 1800589.
[13] J. Li, C. Ge, J. Du, C. Wang, G. Yang, K. Jin, *Adv. Mater.* **2020**, *32*, 1905764.
[14] R. Berdan, T. Marukame, K. Ota, M. Yamaguchi, M. Saitoh, S. Fujii, J. Deguchi, Y. Nishi, *Nat. Electron.* **2020**, *3*, 259.
[15] J. Yoon, S. Hong, Y. W. Song, J.-H. Ahn, S.-E. Ahn, *Appl. Phys. Lett.* **2019**, *115*, 153502.
[16] Y. Choi, S. Oh, C. Qian, J.-H. Park, J. H. Cho, *Nat. Commun.* **2020**, *11*, 4595.
[17] H. E. Lee, J. H. Park, T. J. Kim, D. Im, J. H. Shin, D. H. Kim, B. Mohammad, I.-S. Kang, K. J. Lee, *Adv. Funct. Mater.* **2018**, *28*, 1801690.
[18] B. J. Choi, A. C. Torrezan, J. P. Strachan, P. G. Kotula, A. J. Lohn, M. J. Marinella, Z. Li, R. S. Williams, J. J. Yang, *Adv. Funct. Mater.* **2016**, *26*, 5290.
[19] Y. Yang, Z. Xi, Y. Dong, C. Zheng, H. Hu, X. Li, Z. Jiang, W.-C. Lu, D. Wu, Z. Wen, *ACS Appl. Mater. Interfaces* **2020**, *12*, 56300.
[20] B. Max, M. Hoffmann, H. Mulaosmanovic, S. Slesazeck, T. Mikolajick, *ACS Appl. Electron. Mater.* **2020**, *2*, 4023.
[21] D. A. Dua, C. Graffi, *UCI Machine Learning Repository*, [http://archive.ics.uci.edu/ml]. University of California, School of Information and Computer Science,Irvine, CA **2019**.
[22] C. C. Y. LeCun, C. J. Burges. *The MNIST Database of Handwritten Digits* [Online]. Available: http://yann.lecun.com/exdb/mnist.
[23] Z. Wen, C. Li, D. Wu, A. Li, N. Ming, *Nat. Mater.* **2013**, *12*, 617.
[24] Z. Xi, J. Ruan, C. Li, C. Zheng, Z. Wen, J. Dai, A. Li, D. Wu, *Nat. Commun.* **2017**, *8*, 15217.
[25] C. Zacharaki, P. Tsipas, S. Chaitoglou, S. Fragkos, M. Axiotis, A. Lagoyiannis, R. Negrea, L. Pintilie, A. Dimoulas, *Appl. Phys. Lett.* **2019**, *114*, 112901.
[26] S. M. Yang, J.-G. Yoon, T. W. Noh, *Curr. Appl. Phys.* **2011**, *11*, 1111.
[27] A. Chouprik, M. Spiridonov, S. Zarubin, R. Kirtaev, V. Mikheev, Y. Lebedinskii, S. Zakharchenko, D. Negrov, *ACS Appl. Electron. Mater.* **2019**, *1*, 275.
[28] Y. Noh, M. Jung, J. Yoon, S. Hong, S. Park, B. S. Kang, S.-E. Ahn, *Curr. Appl. Phys.* **2019**, *19*, 486.
[29] J. Y. Jo, H. S. Han, J. G. Yoon, T. K. Song, S. H. Kim, T. W. Noh, *Phys. Rev. Lett.* **2007**, *99*, 267602.
[30] P. Buragohain, C. Richter, T. Schenk, H. Lu, T. Mikolajick, U. Schroeder, A. Gruverman, *Appl. Phys. Lett.* **2018**, *112*, 222901.
[31] A. Chanthbouala, V. Garcia, R. O. Cherifi, K. Bouzehouane, S. Fusil, X. Moya, S. Xavier, H. Yamada, C. Deranlot, N. D. Mathur, M. Bibes, A. Barthélémy, J. Grollier, *Nat. Mater.* **2012**, *11*, 860.
[32] S. Boyn, J. Grollier, G. Lecerf, B. Xu, N. Locatelli, S. Fusil, S. Girod, C. Carrétéro, K. Garcia, S. Xavier, J. Tomas, L. Bellaiche, M. Bibes, A. Barthélémy, S. Saïghi, V. Garcia, *Nat. Commun.* **2017**, *8*, 14736.
[33] A. Gruverman, B. J. Rodriguez, C. Dehoff, J. D. Waldrep, A. I. Kingon, R. J. Nemanich, J. S. Cross, *Appl. Phys. Lett.* **2005**, *87*, 082902.
[34] T. Y. Lee, K. Lee, H. H. Lim, M. S. Song, S. M. Yang, H. K. Yoo, D. I. Suh, Z. Zhu, A. Yoon, M. R. MacDonald, *ACS Appl. Mater. Interfaces* **2018**, *11*, 3142.
[35] M. C. Chun, S. Park, S. Park, G.-y. Park, M. J. Kim, Y. Cho, B. S. Kang, *J. Alloys Compd.* **2020**, *823*, 153777.

[36] W. J. Merz, *Phys. Rev.* **1954**, *95*, 690.
[37] C. Ma, Z. Luo, W. Huang, L. Zhao, Q. Chen, Y. Lin, X. Liu, Z. Chen, C. Liu, H. Sun, X. Jin, Y. Yin, X. Li, *Nat. Commun.* **2020**, *11*, 1439.
[38] S. Oh, T. Kim, M. Kwak, J. Song, J. Woo, S. Jeon, I. K. Yoo, H. Hwang, *IEEE Electron Device Lett.* **2017**, *38*, 732.
[39] H. Ryu, H. Wu, F. Rao, W. Zhu, *Sci. Rep.* **2019**, *9*, 20383.
[40] S. Agarwal, S. J. Plimpton, D. R. Hughart, A. H. Hsia, I. Richter, J. A. Cox, C. D. James, M. J. Marinella, presented at 2016 Int. Jt. Conf. on Neural Networks (IJCNN), Vancouver, British Columbia, Canada, 24–29 July **2016**.
[41] Y. Bengio, in *Neural Networks: Tricks of the Trade*, 2nd ed. (Eds: G. Montavon, G. B. Orr, K.-R. Müller), Springer, Berlin Heidelberg **2012**, p. 437.